Mixed incorporation of carbon and hydrogen in silicate melts under varying pressure and redox conditions

Bijaya B. Karki [a,b,c,*], Dipta B. Ghosh [a,b], Dipendra Banjara [a]

[a] *School of Electrical Engineering and Computer Science, Louisiana State University, Baton Rouge, LA 70803, USA*
[b] *Department of Geology and Geophysics, Louisiana State University, Baton Rouge, LA 70803, USA*
[c] *Center for Computation and Technology, Louisiana State University, Baton Rouge, LA 70803, USA*

ARTICLE INFO

ABSTRACT

Volatiles including carbon and hydrogen are generally considered to be more soluble in silicate melts than in mantle rocks. How these melts contribute to the storage and distribution of key volatiles in Earth's interior today and during its early evolution, however, remains largely unknown. It is essential to improve our knowledge about volatiles-bearing silicate magmas over the entire mantle pressure regime. Here we investigate molten $Mg_{1-x}Fe_xSiO_3$ ($x = 0$, 0.25) containing both carbon and hydrogen using first-principles molecular dynamics simulations. Our results show that the dissolution mechanism of the binary volatiles in melts varies considerably under different conditions of pressure and redox. When incorporated as CO_2 and H_2O components (corresponding to oxidizing conditions) almost all carbon and hydrogen form bonds with oxygen. Their speciation at low pressure consists of predominantly isolated molecular CO_2, carbonates, and hydroxyls. More oxygenated species, including tetrahedrally coordinated carbons, hydrogen (O-H-O) bridges, various oxygen-joined complexes appear as melt is further compressed. When two volatiles are incorporated as hydrocarbons CH_4 and C_2H_6 (corresponding to reducing conditions), hydroxyls are prevalent with notable presence of molecular hydrogen. Carbon-oxygen bonding is almost completely suppressed. Instead carbon is directly correlated with itself, hydrogen, and silicon. Both volatiles also show strong affinity to iron. Reduced volatile speciation thus involves polymerized complexes comprising of carbon, hydrogen, silicon, and iron, which can be mostly represented by two forms: $C_{1-4}H_{1-5}Si_{0-5}O_{0-2}$ (iron-free) and $C_{5-8}H_{1-8}Si_{0-6}Fe_{5-8}O_{0-2}$. The calculated partial molar volumes of binary volatiles in their oxidized and reduced incorporation decrease rapidly initially with pressure and then gradually at higher pressures, thereby systematically lowering silicate melt density. Our assessment of the calculated opposite effects of the volatile components and iron on melt density indicates that melt-crystal density crossovers are possible in the present-day mantle and also could have occurred in early magma ocean environments. Melts at upper mantle and transition zone conditions likely dissolve carbon and hydrogen in a wide variety of oxidized and non-oxygenated forms. Deep-seated partial melts and magma ocean remnants at lower mantle conditions may exsolve carbon as complex reduced species possibly to the core during core-mantle differentiation while retaining a majority of hydrogen as hydroxyls-associated species.

1. Introduction

Volatiles such as carbon and hydrogen are abundant at the Earth's surface and likely exist underneath the surface in significant amounts (e.g., Halliday, 2013; Hier-Majumder and Hirschmann, 2017). They are active ingredients to various geophysical and geochemical processes operating throughout the Earth's history because of their large influences on the properties and behavior of materials that make up our planet (e.g., Dasgupta and Hirschmann, 2010; Litasov and Shatskiy, 2018; Manning, 2018). For instance, the presence of volatiles in minerals and rocks can dramatically lower their melting temperatures thereby widening the incipient melting regime. Volatiles behave incompatibly during melting and are preferably partitioned into melt. This can alter the degree of polymerization and the composition of the resulting melts and hence influence their properties, for example, decreasing the density and viscosity and increasing the electrical conductivity.

Seismic and magnetotelluric observations support the presence of partial melting, particularly, near the upper mantle-transition

* Corresponding author at: School of Electrical Engineering and Computer Science, Louisiana State University, Baton Rouge, LA 70803, USA.

E-mail address: bbkarki@lsu.edu (B.B. Karki).

zone-lower mantle boundaries as well as atop the core-mantle boundary (Revenaugh and Sipkin, 1994; Williams and Garnero, 1996; Toffelmier and Tyburczy, 2007; Liu et al., 2016). Earth would have gone several episodes of melting in its early history due to multiple impacts (Tonks and Melosh, 1993). Subsequent cooling of early magma ocean (Abe, 1997; Rubie et al., 2003) would have contributed to volatile sequestration into the mantle and core. Therefore, we can view melting as a controlling factor to the evolution and distribution of volatiles in the Earth's interior (Hirschmann, 2006; Dasgupta, 2013).

At the ambient pressure, volatiles are usually insoluble in silicate melts, but they become increasingly soluble with increasing pressure (Mysen et al., 1976; Blank et al., 1993; Ardia et al., 2013). The speciation of a given volatile determines its solution mechanism and interaction with silicate components in magmatic liquids. How volatiles are dissolved in melts is sensitive to multiple factors, including pressure, temperature, composition, and oxygen fugacity which all change with depth. The oxidized fluid species are usually considered to be relevant in the upper mantle, transition zone, and subduction regions (Karato, 2011; Dasgupta et al., 2013; Kelemen and Manning, 2015; Sakamaki, 2017) where oxygen fugacity likely takes values above the iron-wüstite (IW) equilibrium by up to 6 log units (Frost, 1991). According to numerous experimental studies, silicate melts incorporate carbon and hydrogen primarily as carbonates and hydroxyls and to some extent as molecular carbon dioxide and water at low pressures (e.g., Brey, 1976; Stolper, 1982; Nowak et al., 2003; Makhluf et al., 2016). Unlike silicate melts, carbonatitic melts could be generated at shallow depths of up to 250 km and in locally oxidized regions in small amounts (Rohrbach and Schmidt, 2011). Reducing conditions are expected to exist in deeper mantle and during accretion stage (Righter and Drake, 1999; Frost and McCammon, 2008). For instance, oxygen fugacity could have been IW-2 log units at the time of core formation when metallic melt was in equilibrium with magma ocean (O'Neill, 1991). Our knowledge of possible reduced species, such as CO, molecular hydrogen, methane, and complex hydrocarbons is so far limited to low pressures (e.g., Mysen et al., 2011).

First-principles computations were instead previously performed to investigate either CO_2- or H_2O-bearing molten silicates over the entire mantle pressure regime (Mookherjee et al., 2008; Karki et al., 2010; Bajgain et al., 2015; Vuilleumier et al., 2015; Ghosh et al., 2017; Solomatova et al., 2019). Here, we consider binary volatiles CO_2+H_2O in pure and iron-bearing $MgSiO_3$ liquids. Low-pressure experiments have implied that such mixed incorporation can influence the incipient melting regime and melt compositional space (Litasov and Shatskiy, 2018; Manning, 2018). More work is needed to understand how these volatiles dissolve in silicate melts and how the stability of volatile-rich mixtures changes under different redox conditions over pressure-temperature ranges relevant to Earth's interior. In particular, the possibility of exsolving volatile species by melts have been suggested under reducing conditions (Mysen et al., 2011; Stagno et al., 2013). To explore possible reduced fluid species over much extended pressure regime, we also study the incorporation of carbon and hydrogen as hydrocarbons. The cases of CO_2+H_2O and hydrocarbons, respectively, correspond to relatively oxidizing and reducing conditions of mantle relevance with their respective oxygen fugacity values perhaps lying above and approaching (or below) the IW equilibrium. Simulation results allow us to assess how these volatiles are correlated in terms of their speciation and their influence on melt properties, particularly density. We also present the implications of our results for the storage and distribution of carbon and hydrogen in Earth today and during its early evolution.

2. Methodology

First-principles molecular dynamics (FPMD) simulations of several volatile-bearing silicate melts were performed using generalized gradients approximation (GGA) and projector augmented wave method as implemented in VASP (Kresse and Furthmüller, 1996). For oxidized incorporation, we used the supercell consisting of $32MgSiO_3+8CO_2+8H_2O$ (total 208 atoms), which corresponds to 10.91 wt% of carbon dioxide (or 2.98 wt% carbon) and 4.46 wt% of water (or 0.5 wt% hydrogen). On the other hand, the supercell consisted of $32MgSiO_3+4CH_4+2C_2H_6$ (total 196 atoms) for reduced incorporation of 2.97 wt% carbon and 0.86 wt% hydrogen. To simulate iron-bearing melts, we substituted 8 Mg atoms in the supercell with 8 Fe atoms (with no spin) corresponding to $X_{Fe} = Fe/(Mg+Fe) = 0.25$. Volatile-free silicate melts were simulated using the 160-atom supercells corresponding to $32Mg_{1-x}Fe_xSiO_3$ for $x = 0$ and 0.25 and the results are consistent the previous results based on the 80-atom supercells (Karki et al., 2018). We also simulated silicate melt containing CO_2 or H_2O separately using GGA as most previous studies were based on local density approximation (Mookherjee et al., 2008; Bajgain et al., 2015; Ghosh et al., 2017). A plane wave cutoff of 400 eV and Gamma Point Brillouin zone sampling were used. Pulay stress varying between 3.5 and 8 GPa over the volume range considered was added to the calculated pressures.

Each melt configuration was thermalized at high temperature (6000 K or above) and then quenched down to desired lower temperatures. We chose thermodynamic conditions so as to ensure that our simulations represented a normal or near-normal liquid state by carefully avoiding deeply supercooled regime; otherwise unusually long simulation runs would be needed to obtain well-converged results. Many canonical *NVT* simulations were run for durations of 20 to 80 picoseconds depending on volume-temperature conditions using a time step of 1 femtosecond. The liquid state was confirmed in each case by examining radial distribution functions which show the presence of short-range order with no long-range order and mean square displacements which show that atoms cover on average distances of at least 5 Å. We simulated all melt systems at 2000 K and near-zero pressure, but our simulations extend pressure up to 100 GPa at 3000 K and cover higher pressures at 4000 K. While GGA was used for all simulations, we also assessed the effects of the Hubbard term with $U = 5$ and $J = 1$ eV (Jang et al., 2017) for iron-bearing melts at selected conditions, which turned out to be relatively small (discussed later).

3. Results and analysis

3.1. Equation of state

The calculated pressure-density (volume)-temperature results of pure $MgSiO_3$ melt and all other melt compositions considered in this study (Fig. S1 and Table S1) can be adequately represented using the following relation:
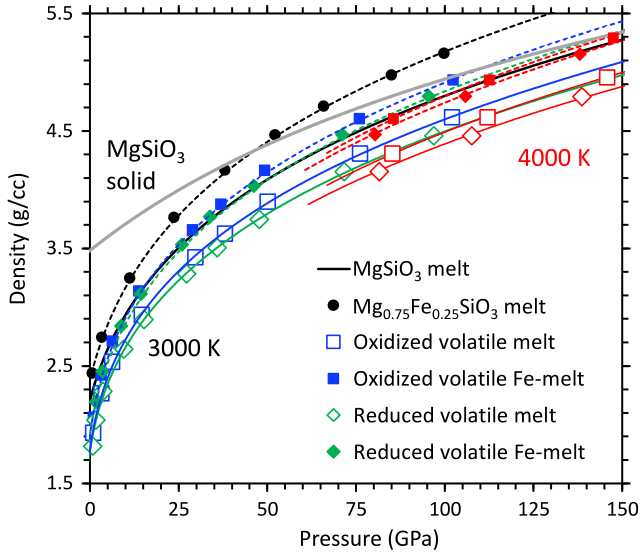
$$P(\rho, T) = P(\rho, T_0) + B(\rho)(T - T_0)$$

Here, the reference isotherm $P(\rho, T_0)$ with $T_0 = 3000$ K is fit to a fourth-order Birch Murnaghan equation of state, whose parameters are given in Table 1 for all melt systems. Because the volatile components are highly compressible, all volatiles-bearing melts are more compressible than the pure melt. This behavior is manifested by the systematically lower values of their zero-pressure bulk modulus. The density-pressure profiles become almost parallel with the pure melt profile at pressures above 50 GPa (solid curves in Fig. 1). The effects of temperature are modeled using

Table 1
Equation of state parameters at 3000 K for pure and four volatiles-bearing silicate melts. Note that the pure melt assumes a quadratic volume dependence for the thermal pressure coefficient.

	$32MgSiO_3$	$32MgSiO_3 +$ $8CO_2$ (2.7 wt% C)	$32MgSiO_3 +$ $16H_2O$ (0.91 wt% H)	$32MgSiO_3 +$ $8CO_2 + 8H_2O$ (2.98 wt% C and 0.5 wt% H)	$32MgSiO_3 +$ $4CH_4 + 2C_2H_6$ (2.97 wt% C and 0.86 wt% H)
ρ_0 (g cm^{-3})	2.209	1.873	1.772	1.785	1.787
V_0 (Å^3)	2415	3160	3280	3450	3100
K_0 (GPa)	19.1 ± 1.6	6.7 ± 0.7	8.2 ± 0.8	7.9 ± 0.7	9.4 ± 0.6
K_0'	4.0 ± 0.1	6.2 ± 0.8	4.9 ± 0.5	5.0 ± 0.5	4.7 ± 0.3
K_0'' (GPa^{-1})	-0.08 ± 0.04	-1.52 ± 0.65	-0.49 ± 0.22	-0.59 ± 0.30	-0.41 ± 0.08
a	35	22	22	20	20
b	-70 ($c = 36$)	-31	-32	-27	-30

Fig. 1. Calculated density-pressure results of $32MgSiO_3+8CO_2+8H_2O$ melt (oxidized volatile incorporation, open squares) and $32MgSiO_3+4CH_4+2C_2H_6$ melt (reduced volatile incorporation, open diamonds) at 3000 K (0 to 100 GPa) and 4000 K (80 to 150 GPa) compared to pure MgSiO$_3$ melt. Solid curves represent the equation of state fits. The corresponding iron-bearing cases are shown by small filled symbols and dashed curves. Also shown is the density-pressure profile of pure MgSiO$_3$ solid at 3000 K.

$B(\rho) = a + b \left(\frac{\rho_0}{\rho} \right)$ for the thermal pressure coefficient, where the zero-pressure density ρ_0 and the parameters a and b for different volatile-bearing melts are given in Table 1. The model curves appear to accurately describe the calculated 4000 K results over the high-pressure regimes considered in this study (Fig. 1 and Fig. S1).

When iron is incorporated in pure and volatiles-bearing silicate melts by substituting Mg atoms with Fe atoms, their volumes change slightly (Fig. S1). Iron content raises melt density mainly for mass reason (Fig. 1, Table S1). The calculated density data of all iron-bearing melts tend to lie slightly above the density-pressure profiles based on the pressure-volume equation of state of the corresponding iron-free melts (dashed curves in Fig. 1). Also note that all volatile-bearing melts are less dense than the corresponding volatile-free melts, consistent with experimental data (Ghosh et al., 2007; Sakamaki, 2017). For the amounts of carbon and hydrogen considered here, the volatile-induced changes in the melt density are smaller under oxidizing conditions than under reducing conditions primarily due to excess oxygen content of the oxidized melt.

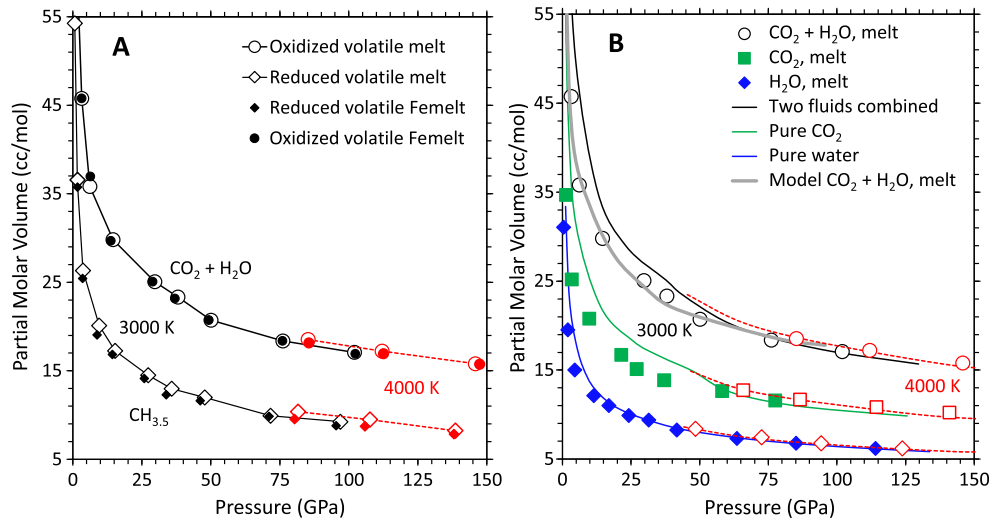### 3.2. Partial molar volumes

We evaluate partial molar volume of a given volatile component from the difference between the volumes of the corresponding volatile-bearing (V) and volatile-free (V_f) silicate melts:

$$\overline{V}_{volatile} = (V - V_f) N_A / n$$

where n is the number of the incorporated volatile units (H_2O or CO_2 or H_2O+CO_2 or hydrocarbon units) in the supercell and N_A is Avogadro's number. This definition is expected to work well because the partial molar volume tends to be independent of total volatile concentration, particularly for hydrous melts (Du et al., 2019). Fig. 2A shows the calculated partial molar volume of binary H_2O+CO_2 and that of $CH_{3.5}$ corresponding to $(4CH_4+2C_2H_6)/8$. In each case, the partial molar volume decreases rapidly initially with increasing pressure and then changes more gradually at higher pressures. It increases somewhat with temperature as shown by comparisons between 3000 and 4000 K at high pressures. $\overline{V}_{H_2O+CO_2}$ is larger than $\overline{V}_{CH_{3.5}}$ by a factor of two because of oxygen in the oxidized case. It is remarkable that the presence of iron in melts does not influence the partial molar volumes of both types of volatile components within the computational uncertainties (Fig. 2A) for possible reason discussed later.

For the case of oxidized volatile incorporation, we also evaluate the partial molar volumes of H_2O and CO_2 by considering their separate solution in MgSiO$_3$ melt (Fig. 2B). The calculated results generally agree with the experimental data which tend to be highly scattered though (Ghosh et al., 2007; Sakamaki et al., 2011; Sakamaki, 2017). As expected, $\overline{V}_{CO_2}$ is much larger than $\overline{V}_{H_2O}$ at all conditions. Their pressure evolution follows the similar trend as seen for $\overline{V}_{H_2O+CO_2}$ and $\overline{V}_{CH_{3.5}}$. We also model $\overline{V}_{H_2O+CO_2}$ as a simple sum of $\overline{V}_{H_2O}$ and $\overline{V}_{CO_2}$. The sum values almost overlap with the directly calculated values of $\overline{V}_{H_2O+CO_2}$ at all conditions. This implied linear behavior can be linked to our finding that carbon and hydrogen do not interact much with each other under oxidizing conditions as discussed later. This means that the molar volume of hydrous carbonated silicate melts can be expressed as a weighted average of all component volumes.

Comparison of the calculated partial molar volume of a volatile component in silicate melt with its molar volume in a pure fluid state allows us to assess the nature of mixing between the volatile and silicate melt components. We investigate this issue in the case of oxidized volatiles. As shown in Fig. 2B, $\overline{V}_{H_2O}$ is smaller than the molar volume of the pure water at zero pressure and two volumes approach each other rapidly as pressure increases. The volume of mixing is negative in the narrow pressure regime 0 to 20 GPa, but the melt + water solution becomes nearly ideal at higher pressures. The situation is, however, different with the melt + CO_2 system. The partial molar volume of CO_2 in melt is considerably smaller than its pure volume and a negative volume of mixing extends over a much wider pressure regime up to 50 GPa. The different mixing behavior of two systems can be associated with differences in the structural variations of these fluids with pressure. While the bulk CO_2 behaves as a molecular fluid over an extended pressure interval (0 to ∼40 GPa) compared to the bulk H_2O fluid (0 to ∼15 GPa), both volatile components take dissociated forms (that is, they are incorporated chemically as carbonate groups, hydroxyls, -O-H-O-) in silicate melt at all pressures (discussed later).

Fig. 2. A. Partial molar volume of binary CO_2+H_2O (oxidized volatiles) and $CH_{3.5}$ (reduced volatiles) as a function of pressure at 3000 and 4000 K without iron (open symbols) and with iron (small filled symbols). Comparison shows that iron has almost no effect on the partial molar volume of volatiles. B. Partial molar volumes of binary CO_2+H_2O (circles) and separate CO_2 (squares) and H_2O (diamonds) in iron-free melts compared with the molar volumes of respective pure fluids. Thick curves represent the direct sum of the partial molar volumes of two oxide volatiles.

Our predictions are consistent with previous computational studies (Bajgain et al., 2015; Ghosh et al., 2017). Comparison of $\overline{V}_{H_2O+CO_2}$ with the sum of volumes of pure H_2O and CO_2 fluids as a function of pressure suggests that the hydrous carbonated melt system is non-ideal with its volume of mixing changing from large negative to almost zero at pressures above 50 GPa. Non-ideal mixing of silicate melt and CO_2+H_2O fluids was experimentally implied at low pressures (Papale et al., 2006).

3.3. Radial distribution functions

We compute a full set of partial radial distributions functions (RDFs) to obtain an overall picture of correlations that exist between different atomic species pairs of the melt (Fig. S2 and S3). A first peak is recognizable in most partial RDFs, but the peaks show large variations in their amplitude, shape, and location among different cases. The well-defined Si-O and Mg-O peaks signify dominant charge order in the host melt whereas the O-O peak corresponds to polyhedral arrangements formed by the cations and anions (Fig. S2). The presence of carbon and hydrogen does not have noticeable influence on host melt correlation functions. There are additional pair-wise correlations involving volatile elements, which deserve a further analysis. Under oxidizing conditions, the C-O and H-O functions (Fig. 3A) show sharp first peaks at distances (1.23 and 0.98 Å, respectively) shorter than the Si-O peak distance (1.62 Å) at zero pressure. Such strong correlations actually imply direct oxygen-bonding of both volatile elements. The C/H-anion correlations remain strong with increasing pressure though the peaks slightly broaden and shift to larger distances. Other volatile-involved RDFs, in particular, C-H, C-C, H-H and C-Si correlations tend to develop a peak/shoulder at elevated pressures (Fig. S2). Our results thus imply that oxygen bonding essentially controls the speciation and dissolution mechanisms of CO_2 and H_2O at all pressures as in the cases when either of these volatile components is separately incorporated in silicate melts (Karki et al., 2010; Bajgain et al., 2015; Ghosh et al., 2017; Solomatova et al., 2019; Du et al., 2019).

The calculated radial distribution functions under reducing conditions show that the H-O correlation is suppressed yet remaining strong, but the direct C-O correlation (as reflected by the first peak) weakens considerably (Fig. 3A, inset). Instead the C-C, C-H and C-Si functions all show sharp peaks at short distances of 1.27,
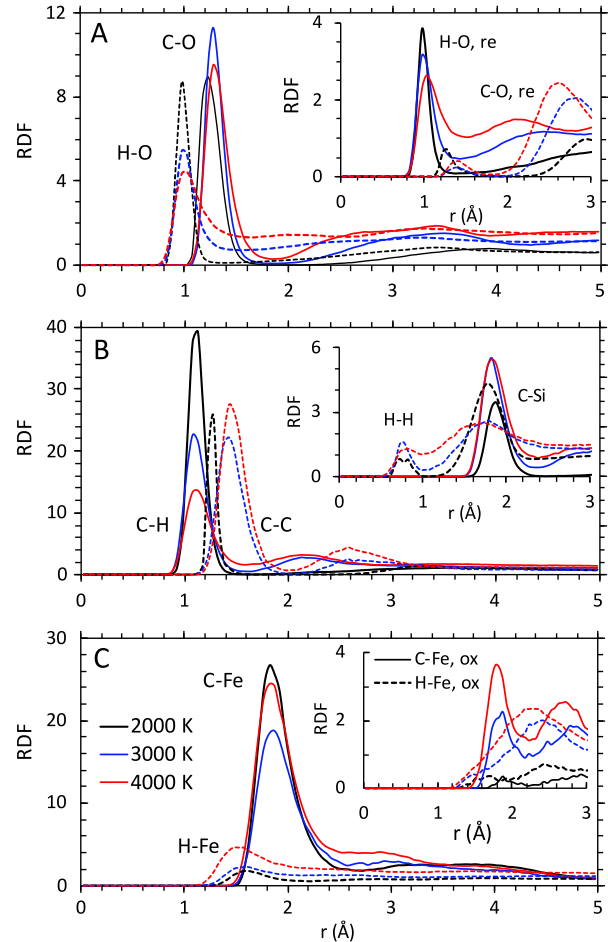
Fig. 3. Volatile-involved radial distribution functions (RDFs) of CO_2+H_2O (oxidized) and hydrocarbons (reduced) bearing silicate melts at 2000 K (0.2 and 0.7 GPa) shown by black curves, at 3000 K (29.7 and 27.3 GPa) by blue curves and at 4000 K (112.0 and 107.6 GPa) shown by red curves. A: Volatile-oxygen functions with the reduced melt results shown in inset. B: Carbon-hydrogen, carbon-carbon, hydrogen-hydrogen and carbon-silicon functions for the reduced melt. C: Volatile-iron functions for the iron-bearing reduced melt (the oxidized results shown in inset). (For interpretation of the colors in the figure(s), the reader is referred to the web version of this article.)

1.12, and 1.87 Å, respectively, at zero pressure. Also noticeable are the H-H (0.82 Å) and H-Si (1.48 Å) peaks (Fig. 3B). The C-O peak around 1.27 Å further weakens with increasing pressure, almost disappearing at high pressure and instead a second peak becomes prominent at a larger distance (Fig. 3A, inset). The H-O RDF and all other volatile-involved RDFs continue to show sharp first peaks on compression. These together imply that volatile elements in reduced melt are highly correlated with each other while direct C-O bonding activity is dramatically suppressed.

Interestingly, iron is directly correlated with both volatiles, particularly with carbon. Under reducing conditions, the C-Fe peak located around 1.83 Å is strong and the H-Fe peak located at 1.5-1.6 Å is noticeable at all pressures (Fig. 3C). Iron tends to enhance the hydrogen-oxygen correlation while suppressing the C-H and C-Si correlations. Under oxidizing conditions, the C-Fe peak is weak and the H-Fe peak is almost absent (Fig. 3C, inset). Iron like other cations is strongly correlated with anion. Interestingly, the Fe-Fe RDF shows a peak at 2.3-2.5 Å whereas all other cation-cation peaks are located at larger distances (Fig. S4). We find that these iron-involved correlations are somewhat sensitive to the use of Hubbard U term; while the Fe-O peak is enhanced, the Fe-Fe peak becomes weaker and also shifts to larger distance. Nevertheless, the predicted strong direct C-Fe correlation (by both GGA and GGA+U calculations) under reducing conditions hints some sort of carbon-iron clustering. Unlike other cations, magnesium is weakly correlated with both volatile elements (Fig. S2 and S3) though the C-Mg and H-Mg peaks tend to become sharper and shift to smaller distances as pressure increases.

3.4. Coordination environments

We evaluate coordination environments of different atomic species pairs by using the distance to the minimum after the first peak in their respective radial distribution functions (Fig. 3) as the cutoff distance. The mean coordination number of atomic species α with respect to atomic species β is denoted by $Z_{\alpha\beta}$, where α and β represent elements Mg, Si, O, C, H, and Fe present in melt composition under consideration.

Oxidized volatile incorporation. As shown in Fig. 4A, the mean oxygen coordination number of carbon (Z_{CO}) of the oxidized melt increases from 2.5 to 3.5 as pressure increases from zero to $\sim$140 GPa. This appears to reflect a mixture of two- and three-fold coordination states at low pressure, which gradually picks up four-fold coordination state mainly at the cost of two-oxygen coordinated carbon atoms at higher pressure. On the other hand, the mean hydrogen-oxygen coordination number (Z_{HO}) increases from 1 to 2 over the same pressure range, signifying the dominance of hydroxyls at low pressure and the appearance of O-H-O groups at high pressure. Each volatile-involved coordination consists of two or more states whose relative abundances are sensitive to pressure, temperature, and composition (Table 2, Table S2). Our coordination results for binary oxide volatiles in silicate melts are mostly comparable to the previous computations for separate incorporation of CO_2 (Ghosh et al., 2017; Solomatova et al., 2019) and H_2O (Mookherjee et al., 2008; Bajgain et al., 2015). The C/H-O coordination relationships can be actually considered as direct bonding between volatile elements and oxygen. We further examine these coordination distributions at three *P-T* conditions below (Table 2).

At 0.2 GPa and 2000 K ($V = 3189.51$ Å^3), Z_{CO} is 2.49. All carbon is coordinated with oxygen; two-fold (CO_2) and three-fold (CO_3) states accounting for nearly 95%. Like carbon, all hydrogen is coordinated with oxygen ($Z_{HO} = 1.02$), almost exclusively as one-fold (hydroxyls) and less than 2% two-fold (O-H-O bridges). Pressure systematically enhances volatile-oxygen bonding activity. At 29.7 GPa (3000 K), the principal species is CO_3 (90%) while doubly and tetrahedrally coordinated carbons are also present in small
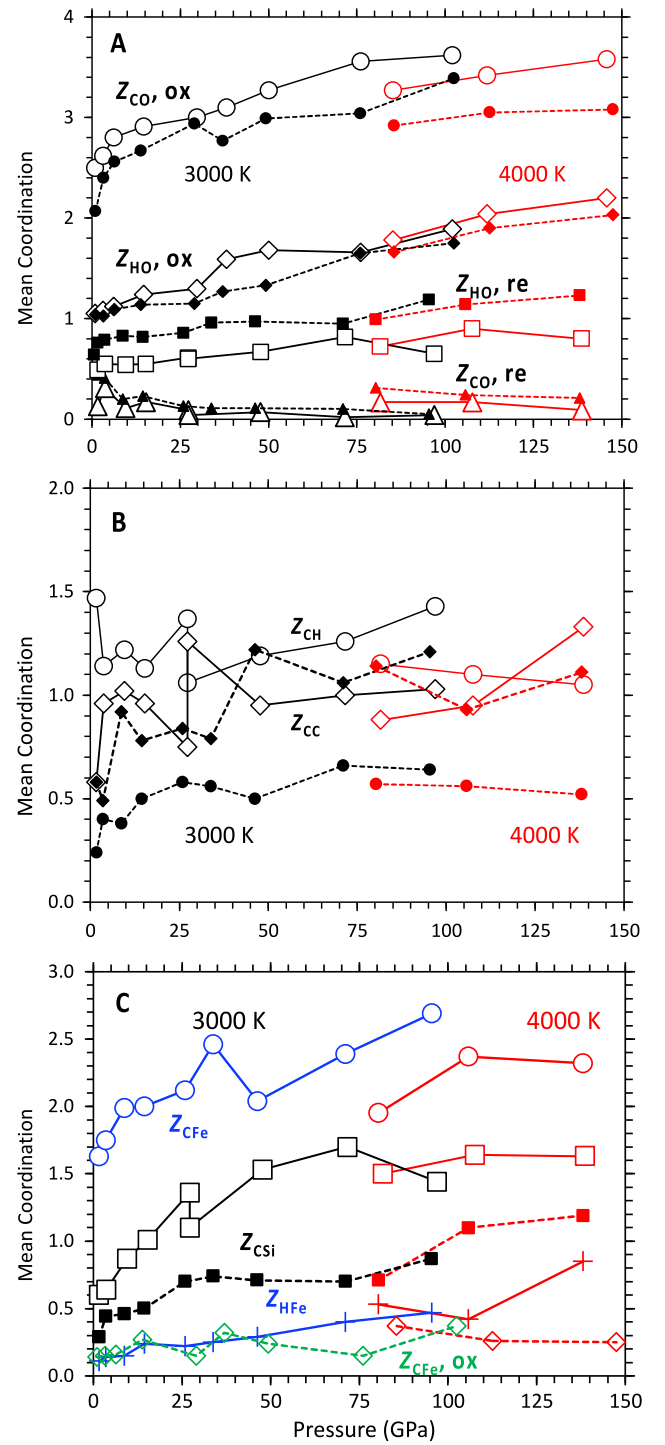
Fig. 4. Calculated mean volatile-involved coordination numbers as a function of pressure at 3000 and 4000 K under oxidizing (**ox**) and reducing (**re**) conditions. Each coordination type is labeled $Z_{\alpha\beta}$ where atomic species α is coordinated with atomic species β. The open and (small) solid symbols denote the results for iron-free and iron-bearing melts, respectively.

amounts. The hydrogen-oxygen coordination consists of decreased yet high proportion of one-fold state ($\sim$70%) and increased proportion of O-H-O bridges ($\sim$30%). As pressure increases further, volatile-oxygen coordination environments change more gradually. At 112 GPa (4000 K), the carbon-oxygen coordination is dominated by CO_3 and CO_4 (together more than 90% carbon participation). A significant fraction of carbon ($\sim$15%) is also coordinated with itself while some carbon is coordinated with hydrogen. The O-H-O

Table 2

Calculated mean numbers and distributions (one-, two-, three- and four-fold states) of volatile-involved coordination in $32MgSiO_3 + 8CO_2 + 8H_2O$ and $32Mg_{0.75}Fe_{0.25}SiO_3 + 8CO_2 + 8H_2O$ melts (corresponding to oxidizing conditions) at three different pressure-temperature conditions. For each coordination type $Z_{\alpha\beta}$ (where atomic species α is coordinated with atomic species β), the first row corresponds to near-zero pressure (2000 K), the second row to $\sim$29 GPa (3000 K), and the third row to $\sim$112 GPa (4000 K).

| Type | CO_2- and H_2O-bearing silicate melts (oxidized case) | | | |
| | Iron-free | | Iron-bearing | |
	Mean	Distribution (%) one, two, three, four	Mean	Distribution (%) one, two, three, four
Z_{CO}	2.49	5.5, 39.9, 54.7, 0	2.19	20.9, 59.4, 29.7, 0
	3.00	0, 5.2, 89.7, 5.1	2.94	1.9, 11.2, 78.4, 8.6
	3.42	0, 6.3, 45.6, 47.9	3.05	3.4, 18.6, 47.6, 30.4
Z_{HO}	1.02	98.3, 1.7, 0, 0	1.01	96.5, 2.1, 0, 0
	1.30	69.7, 30.1, 0.1, 0	1.15	77.3, 18.6, 0, 0
	2.03	15.5, 65.6, 17.9, 0.7	1.90	21.9, 64.2, 12.7, 0.3
Z_{CH}	–	–	–	–
	–	–	0.03	3.3, 0, 0, 0
	0.01	1.3, 0, 0, 0	0.03	2.6, 0, 0, 0
Z_{CC}	–	–	–	–
	–	–	–	–
	0.16	14.7, 0.7, 0, 0	0.31	28.9, 0.8, 0, 0
Z_{CSi}	–	–	–	–
	0.03	3.2, 0, 0, 0	0.03	3.2, 0, 0, 0
	0.05	4.7, 0, 0, 0	0.05	4.7, 0, 0, 0
Z_{CFe}	–	–	0.11	8.5, 1.2, 0, 0
	–	–	0.15	11.0, 1.7, 0, 0
	–	–	0.26	20.6, 2.4, 0, 0
Z_{HFe}	–	–	0.02	1.3, 0.3, 0.1, 0
	–	–	–	–
	–	–	–	–

Table 3

Calculated mean numbers and distributions (one-, two-, three- and four-fold states) of volatile-involved coordination in $32MgSiO_3 + 4CH_4 + 2C_2H_6$ and $32Mg_{0.75}Fe_{0.25}SiO_3 + 4CH_4 + 2C_2H_6$ melts (corresponding to reducing conditions) at three different pressure-temperature conditions. For each coordination type $Z_{\alpha\beta}$ (where atomic species α is coordinated with atomic species β), the first row corresponds to near-zero pressure (2000 K), the second row to $\sim$27 GPa (3000 K), and the third row to $\sim$107 GPa (4000 K).

| Type | Hydrocarbon-bearing silicate melts (reduced case) | | | |
| | Iron-free | | Iron-bearing | |
	Mean	Distribution (%) one, two, three, four	Mean	Distribution (%) one, two, three, four
Z_{CO}	0.16	9.6, 3.1, 0, 0	0.23	25, 0, 0, 0
	0.09	9.1, 0, 0, 0	0.16	8.1, 3.7, 0.1, 0
	0.17	13.3, 1.8, 0, 0	0.24	14.1, 3.2, 1.2, 0
Z_{HO}	0.40	37.6, 1.1, 0, 0	0.65	59.7, 2.1, 0, 0
	0.61	43.7, 8.5, 0, 0	0.85	50, 17.3, 0, 0
	0.90	35.8, 25.9, 0.8, 0	1.14	36.1, 35.5, 2.1
Z_{CH}	1.87	19.5, 26.7, 13.1, 18.6	0.65	10.5, 28.4, 4.4, 0
	1.37	43.4, 30.4, 10.5, 0.3	0.66	25.2, 17.1, 1.9, 0.2
	1.10	41.7, 23.3, 6.1, 0.7	0.56	33.1, 9.0, 1.3, 0.1
Z_{CC}	0.25	25.0, 0, 0, 0	0.46	26, 0, 0, 0
	0.75	49.7, 12.5, 0, 0	0.73	55.2, 8.8, 0.1, 0
	0.95	56.9, 16.7, 1.7, 0	0.93	43.9, 21.9, 1.7, 0
Z_{CSi}	0.75	27.0, 23.9, 0, 0	0.25	12.9, 12.5, 0, 0
	1.36	44.7, 35.6, 3.7, 2.2	0.81	36.7, 20.6, 0.9, 0
	1.64	33.2, 31.6, 16.3, 4.7	1.10	46.9, 22.6, 5.7, 0.3
Z_{CFe}	2.11	17.8, 15.6, 15.0, 25.6	2.11	17.8, 15.6, 15.0, 25.6
	1.87	14.8, 21.2, 17.6, 16.9	1.87	14.8, 21.2, 17.6, 16.9
	2.37	17.8, 27.9, 24.1, 22.1	2.37	17.8, 27.9, 24.1, 22.1
Z_{HFe}	0.12	5.9, 2.8, 0.8, 0	0.12	5.9, 2.8, 0.8, 0
	0.20	9.9, 3.0, 0.9, 0	0.20	9.9, 3.0, 0.9, 0
	0.42	18.2, 8.0, 2.1, 0	0.42	18.2, 8.0, 2.1, 0

bridges and three-oxygen coordinated hydrogens prevail at the cost of individual hydroxyls. Highly compressed melts also contain doubly carbon- and hydrogen-coordinated oxygens in small amounts of 0.6 and 2.5%, respectively (Table S2), which means that some coordination groups are connected with each other.

Reduced volatile incorporation. The coordination environments of carbon and hydrogen in silicate melts become more complex under reducing conditions compared to oxidizing conditions (Table 3, Table S3). The hydrocarbon incorporation suppresses the carbon-oxygen coordination to almost non-existent; Z_{CO} lies below 0.3 at all pressures (Fig. 4A). On the other hand, Z_{HO} is decreased to almost half compared to the oxidized melt. We find that the mean coordination numbers of carbon with respect to itself (Z_{CC}), hydrogen (Z_{CH}), and silicon (Z_{CSi}) all take large values and they tend to increase with pressure (Fig. 4B, 6C). This implies that carbon takes polymerized forms in reduced melt at all pressures. Consistently, hydrogen is highly coordinated with carbon; Z_{HC} takes values between 0.3 and 0.5. Hydrogen is bonded with itself and silicon to much lesser extent; Z_{HH} varies from 0.02 to 0.06 and Z_{HSi} varies from 0.04 to 0.1 over the full pressure range considered. Non-oxygen bonding/coordination of volatile elements which is almost absent under oxidizing conditions thus becomes important under reducing conditions. All these volatiles-involved coordination types show different states, whose relative abundances vary with pressure, temperature, and composition (Table S3).

At 0.7 GPa and 2000 K ($V = 2715.87$ Å^3), only about 13% carbon (as mostly CO and some CO_2) and about 39% hydrogen (as mostly hydroxyls and some O-H-O) are coordinated with oxygen in the reduced melt (Table 3) compared to their full involvement in the oxidized melt (Table 2). This C/H-O undercoordination is compensated by self-coordinated dimers (C_2 and H_2) and various hydrocarbon species (CH, CH_2, CH_3 and CH_4 in comparable pro-

portions). Nearly half of carbon is singly and doubly coordinated with silicon. On the other hand, hydrogen is highly coordinated with carbon (more than half hydrogen participation) and somewhat with silicon and hydrogen. The corresponding coordination numbers are: $Z_{HC} = 0.53$, $Z_{HSi} = 0.04$, and $Z_{HH} = 0.02$. It is interesting to note that the combined value considering all coordination types is 3.02 for carbon and 0.99 for hydrogen for the reduced melt, compared to $Z_{CO} = 2.49$ and $Z_{HO} = 0.99$ under oxidizing conditions.

At 27.3 GPa (3000 K), more than half of carbon is bonded with each other, some taking two-fold coordination state (Table 3). The carbon-hydrogen coordination distribution consists of lower coordination states (in particular, CH and CH_2) in higher proportions owing mainly to increased carbon-silicon coordination when compared to zero pressure. Nearly half of hydrogen forms hydroxyls and O-H-O bridges while the rest contributes to coordination with carbon, itself, and silicon ($Z_{HC} = 0.39$, $Z_{HH} = 0.04$, $Z_{HSi} = 0.06$). At 107.6 GPa (4000 K), carbon is mostly bonded with each other, hydrogen, and silicon (more than 70% carbon participation in each coordination type) but much less with oxygen. A majority of hydrogen is bonded with oxygen. Less than half of hydrogen is coordinated with others ($Z_{HC} = 0.31$, $Z_{HH} = 0.06$, and $Z_{HSi} = 0.07$), mostly in one-fold coordination state (Table S3).

Effects of iron. Our results show that iron content influences coordination environments of volatiles in silicate melts to different extents depending on redox condition (Tables S2 and S3). Iron decreases both Z_{CO} and Z_{HO} of the oxidized melt at all pressures (Fig. 4A). This coordination suppression appears to arise because both volatile elements (in particular, carbon) are also coordinated with iron to some extent. At 0 GPa and 2000 K, about 10% carbon is directly bonded with Fe. As a consequence, more CO and CO_2 and less CO_3 are present resulting in a lower value of $Z_{CO} = 2.09$
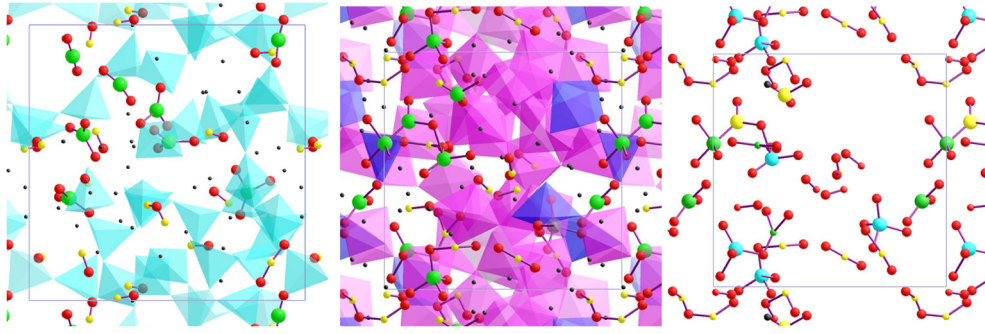
Fig. 5. Visualization snapshots of $32MgSiO_3+8CO_2+8H_2O$ melt at 0.2 GPa and 2000 K (left) and 112 GPa and 4000 K (center and right). The corresponding supercell lengths are 14.72 and 11.01 Å. The SiO_n polyhedra are color-coded: $n = 4$ (cyan), 5 (blue), 6 (magenta) and 7 (white) and Mg atoms appear as black dots. Carbon (large green spheres) and hydrogen (small yellow spheres) are bonded with oxygen (medium red spheres). The volatile speciation at near-zero pressure consists of three CO_2, five CO_3, thirteen hydroxyls, one -O-H-O-, and one molecular water. On right, the color of large and small spheres encodes oxygen-neighbor counts of carbon and hydrogen, respectively (black = 0, red = 1, yellow = 2, green = 3, cyan = 4). At high pressure, there are CO_3, CO_4, HCO_2, CO_4-$HO_{1,2}$, C_2O_5-CO_3 and five hydroxyls (other hydroxyls join to form three-to five-atom sequences).

compared to the iron-free case (Table 2, Table S2). The effects of iron on the H-O coordination are relatively small. In contrast to the oxidized melt, iron tends to increase both Z_{CO} and Z_{HO} of the reduced melt (Fig. 4A). Interestingly, both carbon and hydrogen are coordinated with one or more iron atoms (Table 3, Table S3). Over the full pressure range considered, Z_{CFe} varies between 1.6 and 2.8 whereas and Z_{HFe} varies between 0.1 and 0.8 (Fig. 4C). This high carbon-iron coordination activity (involving around 80% carbon and almost all iron) implies a clustering tendency of carbon with iron, which has been also suggested by recent first-principles simulations of pyrolytic melt + CO system (Solomatova et al., 2019). Another consequence of this is to lower Z_{CSi} and Z_{CH} to almost half of their values in the absence of iron (Figs. 4B, 4C). As hydrogen is less coordinated with carbon compared to the iron-free case, the hydrogen-oxygen coordination is considerably enhanced under reducing conditions.

Host cation-anion coordination. The addition of CO_2 and H_2O in silicate melts tends to slightly enhance the mean magnesium-oxygen coordination because volatile-contributed oxygen (labeled as O_{vol}) forms bond with magnesium, that is, $MgO_n + O_{vol} \leftrightarrow MgO_{n+1}$ (Fig. S5). Mean Si-O coordination, however, remains unaffected irrespective of iron content (Fig. S5). When O_{vol} gets bonded with silicon by breaking one of its polyhedral bridging oxygen bonds, the coordination state of the concerned silicon does not change and O_{vol} becomes non-bridging oxygen: Si-O-Si + O_{vol} ↔ 2 O-Si (Table S4). On the other hand, the reduced volatile incorporation systematically suppresses both cation-anion coordination environments (Fig. S5). The calculated values of Z_{SiO} are smaller than those for the pure and oxidized melts at all pressures because two- and three-fold coordination states appear in significant amounts in reduced melts (Table S5). Such undercoordinated silicon atoms are also bonded with volatiles. The mean iron-oxygen coordination number is lower than Z_{MgO} in the oxidized case and much lower than Z_{SiO} in the reduced case (Fig. S5) because iron is directly correlated with both carbon and hydrogen. We note that the use of GGA+U considerably increases the mean Fe-O coordination numbers of both oxidized and reduced melts at all pressures (Tables S4, S5) as it tends to suppress direct iron-iron correlations (Fig. S3).

Dissolved volatile components in silicate melts are usually considered to influence the degree of melt polymerization (defined by NBO/Si ratio). Our results show that the mean O-Si coordination number systematically decreases in the presence of CO_2 and H_2O (Fig. S5) mainly because free oxygens, not bonded with any silicon, appear in significant amounts at low pressures (Table S4, S5). More non-bridging oxygens appear as both volatiles get bonded with host melt oxygen thereby breaking up the silicate

network. The result is the depolymerization of melts (i.e., increased NBO/Si). The role of these volatiles in regard to melt polymerization appears to change with increasing pressure. Because of its high oxygen-coordination, carbon tends to behave more as a network former than a network modifier in highly compressed melts. The majority of hydrogen participates in inter-polyhedral bridging (-Si-O-H-O-Si-) and three-fold oxygen coordination state (Table 2). The situation is, however, very different under reducing conditions because the volatiles form bonds with other elements (much more in the case of carbon) besides oxygen (Table S4). This results in fewer free oxygens and more non-bridging and bridging oxygens relative to the oxidized case (Table S5). As such, the hydrocarbon incorporation lowers Z_{OSi} to lesser extent than the oxidized volatile incorporation does. Interestingly, these coordination effects are even smaller in the presence of iron perhaps because of enhanced volatile-iron bonding.

3.5. Volatile speciation

By examining the details of local coordination/bonding environments of carbon and hydrogen, we identify various forms of their speciation in silicate magmas. Under oxidizing conditions, the predicted speciation at low pressure occurs predominantly as carbonates, molecular CO_2, and hydroxyls (Fig. 5, left). These oxidized species in different proportions were experimentally detected in silicate melts and glasses (Stolper, 1982; Fine and Stolper, 1985; Nowak et al., 2003). Other species, including CO, molecular water and O-H-O are present in much lower proportions. All C/H-O groups remain isolated from each other. As pressure increases, carbonate and tetrahedral carbon groups appear in higher abundances. While hydroxyl groups remain prevalent, bridging hydrogen (O-H-O) and four-atom sequence (O-H-O-H) become increasingly important at higher pressures. Some of these oxidized species also join with each other to form mixed groups like CO_3-HO and CO_4-HO when oxygen is shared between carbon and hydrogen. Additional species, such as C_2O_5, HCO_2, $SiCO_3$ where carbon is directly bonded with carbon, hydrogen and/or silicon appear to some extent. Even larger complexes are formed in highly compressed melts. For example, CO_4H-O_2H and C_2O_5-CO_3 exist at 112 GPa (Fig. 5, center and right). Given the prevalence of carbon/hydrogen complexes connected by oxygen, the dissolution mechanisms of CO_2 and H_2O in silicate melts essentially involve oxygen bonding of carbon/hydrogen.

Under reducing conditions, both volatiles besides bonding with oxygen also form bonds with each other and silicon. As a result, the reduced melt shows a richer set of speciation of which majority does not involve oxygen. Visualization reveals CH_4, CH_3, H_2, C_2,
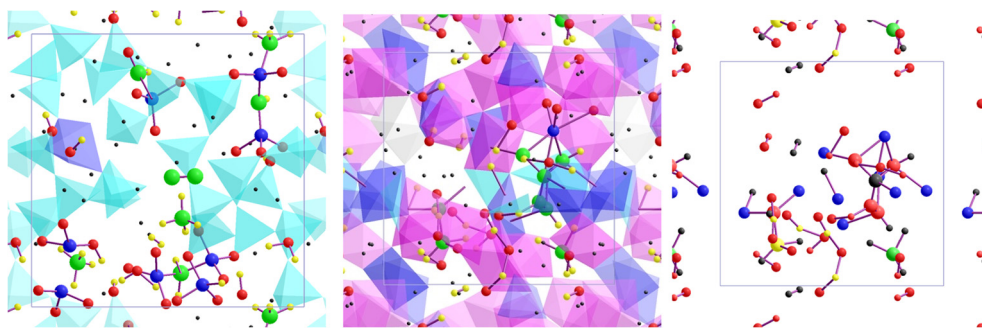
Fig. 6. Visualization snapshots of $32MgSiO_3+4CH_4+2C_2H_6$ melt at 0.7 GPa and 2000 K (left) and 107.6 GPa and 4000 K (center and right). The corresponding supercell lengths are 13.95 and 10.75 Å. The melts consist of SiO_n polyhedra (undercoordinated states appear as blue spheres connected with red spheres) and Mg atoms (black dots). Bonds are shown for carbon (large green spheres) with other carbon, hydrogen (small yellow spheres) and silicon. Hydrogen is bonded with oxygen and carbon. The volatile speciation (on left) consists of CH_4 (two), hydroxyls (six), molecular water (two), H_2, C_2, CH_2Si_2, $CHSiO$, and $C_2H_4Si_2$. On right, the color of large and small spheres encodes the H-neighbor count of carbon and the O-neighbor count of hydrogen, respectively: black = 0, red = 1, yellow = 2, green = 3. Besides one CH_3, six hydroxyls, and two H_2, there exist $C_2H_4Si_2O$, $C_5H_4Si_6$, and three-to-five atom hydroxyl sequences at high pressure.
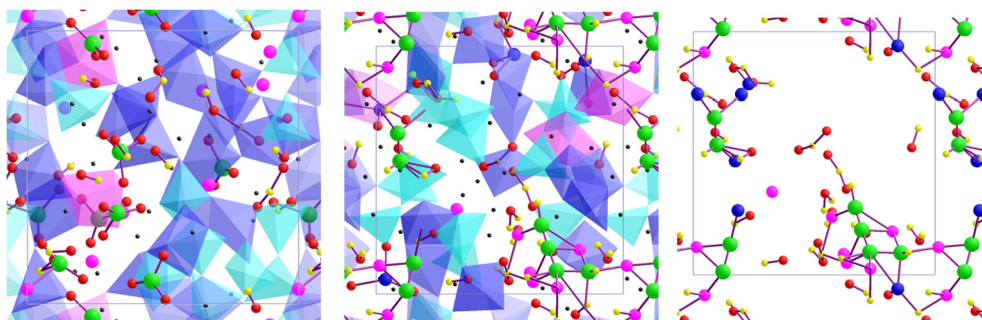
Fig. 7. Visualization snapshots of iron-bearing silicate melts: $32(Mg_{0.75}Fe_{0.25})SiO_3+8CO_2+8H_2O$ at 29.0 GPa (left) and $32(Mg_{0.75}Fe_{0.25})SiO_3+8C+28H$ at 25.9 GPa (center and right), both at 3000 K. The melts consist of SiO_n polyhedra (undercoordinated states appears as blue-red spheres) and Mg atoms (black dots). Links denote the bonding of carbon (large green spheres) and hydrogen (small yellow spheres) with other elements including iron (magenta spheres). In the oxidized melt (left), carbon forms carbonates (six CO_3, one HCO_3Fe, and one $FeCO_3$ groups) and hydrogen forms hydroxyls (twelve OH, two -O-H-O- and one H-O-H-O-). In the reduced melt (center and left), carbon and some hydrogen together form two large complexes $C_2H_2Si_3O$ and $C_6H_7Si_2Fe_6O_2$. Two-third hydrogen appears as OH-involved species. Two iron atoms not bonded with C/H show five- and six-fold oxygen coordination.

HSi, CH_2Si_2 and $C_2H_{4-5}Si_2$ at zero pressure, where silicon is un-dercoordinated (two or three-fold) with oxygen (Fig. 6, left). The predicted methane and methyl groups were detected experimen-tally under reducing conditions at low pressures (Mysen et al., 2011; Ardia et al., 2013). Molecular hydrogen and carbon dimer are not directly correlated with oxygen and silicon and they tend to be highly mobile. The carbon dimer is instead coordinated with two or more Mg atoms and occasionally decorated by hydrogen. Molecular H_2 was experimentally observed in silicate melts un-der controlled hydrogen-fugacity (Hirschmann et al., 2012). On the other hand, oxygen-participated species include mostly hydroxyls and some O-H-O and molecular water as in the oxidized case. They appear in the regions where carbons are absent. When carbon is bonded with oxygen, it is also bonded with silicon and hydrogen to form $CO_{1,2}HSi$ group.

As pressure increases, carbon and hydrogen form larger com-plexes. For instance, single-, double- to triple-carbon groups rep-resented as $C_{1-3}H_{1-5}Si_{1-5}O_{0-1}$ appear at 27.3 GPa and 3000 K. They include CH_2Si, CH_3Si, CH_2Si_2, $CHSi_2O$, $C_2H_2Si_4$, $C_3H_4Si_4$, and $C_3H_5Si_5O$. More than half of hydrogen forms hydroxyls and O-H-O groups and some O-H-O-H and H_2. The reduced-carbon groups are further extended when melt is highly compressed. At 107.6 GPa (4000 K), carbons form dimers and trimers via direct C-C bonding (Fig. 6, center and right). These carbons are also bonded with about one third of silicon as -C-Si-C- and -Si-C-Si- sequences. There are two or three large clusters on average (in our simulated 196-atom supercell), which are decorated mostly with hydrogen and occa-sionally with oxygen. The bonds of carbon with itself, hydrogen and silicon thus together define large complexes of which three-fourth consists of up to four carbons. Larger complexes consisting

of five or more carbons incorporate more silicon and hydrogen: $C_{5-8}H_{4-10}Si_{5-8}O_{0-2}$. The two-third hydrogen is dissolved as oxi-dized species in highly compressed melt.

Iron influences volatile speciation because carbon and to some extent hydrogen also form bonds with iron. The oxidized melt contains some $CO_{1-3}Fe$ and $HCFeO_{1-3}$ in which bonding exists between carbon and each of other elements (Fig. 7, left). On the other hand, the reduced melt involves iron to much greater ex-tent because of stronger iron affinity of both volatiles. Almost all iron is bonded with carbon while a majority of it is bonded with hydrogen (Fig. 7, center and right). The result is large com-plexes like $C_6H_7Si_2O_2Fe_6$ in which oxygen is bonded only with car-bon. Pressure somewhat enhances volatile-iron bonding and silicon participation while suppressing both carbon-oxygen and carbon-hydrogen bonding. We even identify all carbon-all iron cluster, such as $C_8H_7OSi_7Fe_8$ in our simulated system at 105.8 GPa (4000 K), where hydrogen is bonded with carbon and/or iron. Iron-involved clusters mostly consist of five or more carbons whereas iron-free clusters mostly consist of up to four carbons. These clus-ters are further decorated by silicon and hydrogen. While the de-tails of the speciation of carbon and hydrogen under oxidizing and reducing conditions are considerably influenced by the presence of iron, each volatile element appears to be integrated in iron-free and iron-bearing melts to similar degree. The effective local coor-dination of carbon and hydrogen considering all atoms (O, C, H, Si, Fe) with which the volatile atoms are directly bonded remains essentially unchanged (Table S2 and S3). For instance, the total car-bon coordination number varies from ~2.8 to ~4.6 in the pressure range 0 to 100 GPa for iron-bearing melts, irrespective of redox conditions, compared to the corresponding variations of ~2.7 to

~3.9 for iron-free melts. This perhaps explains why iron has almost no influence on the partial molar volume of the H_2O+CO_2 and $CH_{3.5}$ components in silicate melts (Fig. 2a).

4. Implications

We present implications of the calculated results on melt density and volatile speciation for present day partial melting in the mantle and early magma ocean. The issue about possible melt-crystal density crossovers at deep mantle/magma ocean conditions is important (e.g., Agee, 1998; Caracas et al., 2019). Density comparisons between molten and crystalline $MgSiO_3$ imply that such a density crossover does not occur in iso-chemical situations (Fig. 1). The calculated density difference $\Delta\rho = \rho_{melt} - \rho_{crystal}$ remains always negative though its magnitude considerably decreases with pressure: $\Delta\rho = -0.50$ g/cc at 25 GPa (3000 K) and $\Delta\rho = -0.09$ g/cc at 130 GPa (4000 K). However, melt composition is expected to differ considerably from co-existing solid composition because incompatible elements including iron, carbon, and hydrogen preferably partition to melts. It is remarkable that the density of $MgSiO_3$ liquids containing volatiles and iron in amounts considered in our simulated systems actually exceeds the pure solid density; $\Delta\rho$ becomes zero at ~110 and ~140 GPa, respectively, for the oxidized and reduced cases (Fig. 1).

Water-rich mantle transition zone materials may undergo dehydration melting when they are transported to the upper mantle or the lower mantle (Karato, 2011; Schmandt et al., 2014). Volatiles-bearing materials carried by subduction slab (Kelemen and Manning, 2015; Rüpke et al., 2004) may melt when the slab stagnates at a boundary region, probably feeding more volatiles to nearby silicate melts. To assess the stability of these partial melts, we estimate their iron content to be 0.24 by adopting an iron solid/melt partitioning coefficient of 0.35 (Corgne et al., 2005) and a bulk iron content of 0.1 as done previously (Karki et al., 2018). For this excess iron content, our results show that melts with any amounts of volatiles are less dense than coexisting bridgmanite at shallow lower mantle pressures. However, these melts can still be heavier than solid materials which are present in the transition zone. As such, partial melts are likely retained around 660 km depth and can be associated with low-velocity seismic observations (Liu et al., 2016). Since reducing conditions are expected at these depths, our speciation results suggest that carbon forms clusters with carbon, hydrogen, silicon, and iron. Much of carbon may eventually exsolve from melts as diamond, hydrocarbons or carbides as also suggested previously (e.g., Dasgupta and Hirschmann, 2010; Mysen et al., 2011; Stagno et al., 2013). However, melts likely remain hydrous as a majority of hydrogen is dissolved as hydroxyls-associated species.

For partial melting in deepest parts of the mantle, the estimated iron content using an iron partition coefficient value of 0.2 (Tateno et al., 2014) is 0.35. Our results show that partial melts there even with large amounts of volatiles can be denser than co-existing solids and are thus gravitationally stable atop the core-mantle boundary. These deep-seated partial melts may be remnants of early magma ocean (Labrosse et al., 2007). Also, subducted materials upon reaching the bottommost part of the mantle may undergo redox melting as they come in contact with reduced lithologies or metallic iron. Because of reducing conditions there, any primordial or subducted volatiles that may have existed as C-H-Si-Fe complexes and hydroxyls-associated groups (based on our speciation results) likely remain buried in deepest mantle on very long timescales. It is also possible that they are transported partly to the underlying core or partly towards the surface by the mantle plume.

How carbon and hydrogen were incorporated in magma ocean environments could have dictated their subsequent storage and distribution in the Earth's interior. Magma ocean created by the moon forming-giant impact late in accretion (Tonks and Melosh, 1993) is generally considered to be a molten silicate-metal iron system possibly containing a lot of volatiles (e.g., Halliday, 2013; Grewal et al., 2019). Subsequently, magma ocean would have undergone segregation of the core and fractional solidification thus driving major chemical redistribution (Rubie et al., 2003; Monteux et al., 2016). Reducing conditions are expected to have existed during early stages of core formation (e.g., O'Neill, 1991; Righter and Drake, 1999). Based on our volatile speciation results, carbon would be in polymerized forms via C-C, C-H and C-Si bonds while hydrogen would also exist as O-H associated species and molecular hydrogen. Moreover, carbon and to some extent hydrogen because of their affinity to iron would form C-H-Si-Fe clusters. Such volatiles-iron complexes would likely exsolve from magma ocean into sinking metallic liquid. As the core segregation progressed, more reduced (non-oxygenated) species were removed from magma ocean possibly raising its bulk oxygen content. Magma ocean could have been oxidized (relative to the iron-wüstite reference) at depths corresponding to the upper mantle and transition zone when magma ocean and iron-rich core approached chemical equilibrium (Armstrong et al., 2019; Deng et al., 2020). While a majority of carbon seemed to have been transported to the core, a majority of hydrogen would have been retained in magma ocean. A similar scenario has been suggested on the basis of measured partition coefficients of hydrogen and carbon between metal and silicate melts (e.g., Kuramoto and Matsui, 1996; Malavergne et al., 2019).

On cooling, magma ocean would begin to crystallize most likely at mid depths (Stixrude et al., 2009). During fractional solidification, iron and volatiles would be preferably partitioned to silicate melt over crystals. We consider a situation in which half of the magma ocean has crystallized. The estimated iron contents are 0.17 and 0.03 for melt and crystal, respectively (Karki et al., 2018). This corresponds to $\Delta\rho = 0$ at 80 GPa and 0.14 g/cc at 130 GPa for $(Mg,Fe)SiO_3$ with no volatiles. Based on our density results, we find that $\Delta\rho$ becomes zero when up to 2 wt% of carbon and 0.5 wt% of hydrogen are added in silicate melts. This means that iron-enriched melts with significant amounts of volatiles would be sufficiently dense to percolate downwards. The result would be a basal magma ocean as previously suggested (Labrosse et al., 2007; Stixrude et al., 2009; Caracas et al., 2019), which became denser and richer in incompatible elements with time, probably serving as a geochemically enriched reservoir at the bottom of the lower mantle. On the upper side, melt would float and migrate towards the surface. As more oxidizing conditions were expected at shallow depths, carbon and hydrogen would have chemically dissolved in magma ocean via oxygen-bonding and to some extent by bonding with silicon and iron. While upwelling, silicate melts would have crystallized to possibly form hydrous minerals in the transition zone and carbonated phases in the upper mantle. Some volatiles could have exsolved to the then atmosphere while magma ocean was cooling (Elkins-Tanton, 2008; Lebrun et al., 2013; Deng et al., 2020).

5. Conclusions

Though experimental studies of volatiles-bearing silicate melts and glasses are confined to relatively low pressures, recent computational studies have covered much wider pressure ranges. Unlike previous first-principles molecular dynamics simulations, here we have investigated how carbon and hydrogen together are dissolved in pure and iron-bearing $MgSiO_3$ melts and how these volatiles influence melt properties over the entire mantle pressure regime at 2000-4000 K. Two opposite scenarios of redox we have considered represent oxidizing conditions above the iron-wüstite equilibrium ($8CO_2+8H_2O$ incorporation) and reducing conditions approaching

or below the equilibrium (hydrocarbon $4CH_4 + 2C_2H_6$ incorporation). The simulation results allow us to evaluate volume/density-pressure relationships and analyze the behavior of volatile-melt solutions. The calculated partial molar volumes of binary H_2O+CO_2 (oxidized) and $CH_{3.5}$ (reduced) each decreases rapidly initially with increasing pressure and then changes more gradually at higher pressures. Interestingly, $\overline{V}_{H_2O+CO_2}$ is larger than $\overline{V}_{CH_{3.5}}$ by a factor of two and both volumes are almost insensitive to iron content. Our analysis also suggests that $\overline{V}_{H_2O+CO_2}$ can be taken as a simple sum of $\overline{V}_{H_2O}$ and $\overline{V}_{CO_2}$. While carbon and hydrogen lower the melt density, iron raises it. As these opposite effects can be counterbalanced for plausible contents of volatiles and iron, the melt-crystal density crossover is possible when the mantle undergoes partial melting and could have occurred in early magma oceans. This means that dense volatiles-bearing silicate melts can be transported and accumulated at specific depths likely along the compositional or phase boundaries.

Simulated atomic position-time series allow us to analyze pairwise correlations and local coordination environments to infer the speciation and dissolution mechanisms of carbon and hydrogen in silicate melts. Under oxidizing conditions, these volatiles are exclusively bonded with oxygen but are weakly correlated with each other (direct carbon-hydrogen correlation is almost absent). The volatile speciation at low pressure consists of predominantly molecular CO_2, carbonate, hydroxyl, and some molecular water and O-H-O (mostly existing in isolation), consistent with experimental observations. As pressure integrates volatiles more into melts via enhanced oxygen-bonding, more oxygen-involved species appear and also some $CO_{2,3}$ and hydroxyl groups join with each other via oxygen sharing. Both volatiles show weak tendency to polymerize as they rarely form bonds with each other and with other cations, including iron. Under reducing conditions, while hydrogen-oxygen bonding remains strong, direct carbon-oxygen correlation is dramatically suppressed. Instead carbon is highly correlated/bonded with itself, hydrogen and silicon, and both volatiles are also bonded with iron. As such, large complexes containing carbon, hydrogen, and silicon (and iron) become prominent, more so at higher pressures. These species can be mostly represented by two forms: $C_{1-5}H_{1-5}O_{0-2}Si_{0-5}$ (iron-free) and $C_{5-8}H_{1-5}O_{0-2}Si_{0-6}Fe_{6-8}$. Our speciation results suggest that dense partial melts and magma ocean at lower mantle conditions incorporate volatiles as C-H-Si-Fe clusters, probably exsolving most carbon as reduced species but retaining a majority of hydrogen as hydroxyls-associated species. But, melts at upper mantle and transition zone conditions appear to dissolve carbon and hydrogen in a wide variety of oxidized and reduced/non-oxygenated forms. Improved knowledge of the speciation of carbon and hydrogen in silicate melts and their influence on melt density under different conditions of pressure and redox is thus helpful to better understand the incorporation of these volatiles in magma ocean environments and their subsequent storage and distribution in the Earth's interior.

CRediT authorship contribution statement

Bijaya B. Karki: Conceptualization, Supervision, Investigation, Visualization, Writing - original draft. **Dipta B. Ghosh**: Investigation, Discussion, Writing - reviewing and editing. **Dipendra Banjara**: Investigation, Discussion, Writing - reviewing and editing.

Declaration of competing interest

The authors declare that they have no known competing financial interests or personal relationships that could have appeared to influence the work reported in this paper.

Appendix A. Supplementary material

Supplementary material related to this article can be found online at https://doi.org/10.1016/j.epsl.2020.116520.

References

Abe, Y., 1997. Thermal and chemical evolution of the terrestrial magma ocean. Phys. Earth Planet. Inter. 100, 27–39.

Agee, C.B., 1998. Crystal-liquid density inversions in terrestrial and lunar magmas. Phys. Earth Planet. Inter. 107, 63–74.

Ardia, P., Hirschmann, M.M., Withers, A.C., Stanley, B.D., 2013. Solubility of CH_4 in a synthetic basaltic melt, with applications to atmosphere-magma ocean-core partitioning of volatiles and to the evolution of the Martian atmosphere. Geochim. Cosmochim. Acta 114, 52–71.

Armstrong, K., Frost, D.J., McCammon, C.A., Rubie, D.C., Boffa Ballaran, T., 2019. Deep magma ocean formation set the oxidation state of Earth's mantle. Science 365, 903–906.

Bajgain, S., Ghosh, D.B., Karki, B.B., 2015. Structure and density of basaltic melts at mantle conditions from first-principles simulations. Nat. Commun. 6, 8578.

Blank, J.G., Stolper, E.M., Caroll, M.R., 1993. Solubilities of carbon dioxide and water in rhyolitic melt at 850°C and 750 bars. Earth Planet. Sci. Lett. 119, 27–36.

Brey, G., 1976. CO_2 solubility and solubility mechanisms in silicate melts at high pressures. Contrib. Mineral. Petrol. 57, 215–221.

Caracas, R., Hirose, K., Nomura, R., Ballmer, M.D., 2019. Melt–crystal density crossover in a deep magma ocean. Earth Planet. Sci. Lett. 516, 202–211.

Corgne, A., Liebske, C., Wood, B.J., Rubie, D.C., Frost, D.J., 2005. Silicate perovskite-melt partitioning of trace elements and geochemical signature of a deep perovskitic reservoir. Geochim. Cosmochim. Acta 69, 485–496.

Dasgupta, R., Hirschmann, M.M., 2010. The deep carbon cycle and melting in Earth's interior. Earth Planet. Sci. Lett. 298, 1–13.

Dasgupta, R., 2013. Ingassing, storage, and outgassing of terrestrial carbon through geologic time. Rev. Mineral. Geochem. 75, 183–229.

Dasgupta, R., Mallik, A., Tsuno, K., Withers, A.C., Hirth, G., Hirschmann, M.M., 2013. Carbon-dioxide-rich silicate melt in the Earth's upper mantle. Nature 493, 211–215.

Deng, J., Du, Z., Karki, B.B., Ghosh, D.B., Lee, K.L.M., 2020. A magma ocean origin to divergent redox evolutions of rocky planetary bodies and early atmospheres. Nat. Commun. 11, 2007.

Du, Z., Deng, J., Miyazaki, Y., Mao, H.-k, Karki, B.B., Lee, K.L.M., 2019. Fate of hydrous Fe-rich silicate melt in Earth's deep mantle. Geophys. Res. Lett. 46, 9466–9473.

Elkins-Tanton, L., 2008. Linked magma ocean solidification and atmospheric growth for Earth and Mars. Earth Planet. Sci. Lett. 271, 181–191.

Fine, G., Stolper, E., 1985. The speciation of carbon dioxide in sodium aluminosilicate glasses. Contrib. Mineral. Petrol. 91, 105–121.

Frost, B.R., 1991. Stability of oxide minerals in metamorphic rocks. Rev. Miner. 25, 469–488.

Frost, D.J., McCammon, C.A., 2008. The redox state of Earth's mantle. Annu. Rev. Earth Planet. Sci. 36, 389–420.

Ghosh, S., Ohtani, E., Litasov, K., Suzuki, A., Sakamaki, T., 2007. Stability of carbonated magmas at the base of the Earth's upper mantle. Geophys. Res. Lett. 34, L22312.

Ghosh, D.B., Bajgain, S.K., Mookherjee, M., Karki, B.B., 2017. Carbon-bearing silicate melt at deep mantle conditions. Sci. Rep. 7, 848.

Grewal, D.S., Dasgupta, R., Sun, C., Tsuno, K., Costin, G., 2019. Delivery of carbon, nitrogen, and sulfur to the silicate Earth by a giant impact. Sci. Adv. 51, eaau3669.

Halliday, A.N., 2013. The origins of volatiles in the terrestrial planets. Geochim. Cosmochim. Acta 105, 146–171.

Hier-Majumder, S., Hirschmann, M.M., 2017. The origin of volatiles in the Earth's mantle. Geochem. Geophys. Geosyst. 18, 2078–3092.

Hirschmann, M.M., 2006. Water, melting, and the deep Earth H_2O cycle. Annu. Rev. Earth Planet. Sci. 34, 629–653.

Hirschmann, M.M., Withers, A.C., Ardia, P., Foley, N.T., 2012. Solubility of molecular hydrogen in silicate melts and consequences for volatile evolution of terrestrial planets. Earth Planet. Sci. Lett. 345–348, 38–48.

Jang, B.G., Kim, D.Y., Shim, J.H., 2017. Metal-insulator transition and the role of electron correlation in FeO_2. Phys. Rev. B 95, 075144.

Karato, S., 2011. Water distribution across the mantle transition zone and its implications for global material circulation. Earth Planet. Sci. Lett. 301, 413–423.

Karki, B.B., Bhattarai, D., Mookherjee, M., Stixrude, L., 2010. Visualization-based analysis of structural and dynamical properties of simulated hydrous silicate melt. Phys. Chem. Miner. 37, 103–117.

Karki, B.B., Ghosh, D.B., Maharjan, C., Karato, S-i, Park, J., 2018. Density-pressure profiles of Fe-bearing $MgSiO_3$ liquid: effects of valence and spin states, and implications for the chemical evolution of the lower mantle. Geophys. Res. Lett. 45, 3959–3966.

Kelemen, P.B., Manning, C.E., 2015. Reevaluating carbon fluxes in subduction zones, what goes down, mostly comes up. Proc. Natl. Acad. Sci. 112, E3997–E4406.

Kresse, G., Furthmüller, J., 1996. Efficient iterative schemes for ab initio total-energy calculations using a plane-wave basis set. Phys. Rev. B 54, 11169–11186.

Kuramoto, K., Matsui, T., 1996. Partitioning of H and C between the mantle and core during the core formation in the Earth: its implications for the atmospheric evolution and redox state of early mantle. J. Geophys. Res., Planets 101, 14909–14932.

Labrosse, S., Hernlund, J., Coltice, N., 2007. A crystallizing dense magma ocean at the base of the Earth's mantle. Nature 450, 866–869.

Lebrun, T., Massol, H., Chassefière, E., Davaille, A., Marcq, E., Sarda, P., Leblanc, F., Brandeis, G., 2013. Thermal evolution of an early magma ocean in interaction with the atmosphere. J. Geophys. Res., Planets 118, 1155–1176.

Litasov, K.D., Shatskiy, A., 2018. Carbon-bearing magmas in the Earth's deep interior. In: Kono, Y., Sanloup, C. (Eds.), Magmas Under Pressure: Advances in High-Pressure Experiments on Structure and Properties of Melts. Cambridge, pp. 419–453.

Liu, Z., Park, J., Karato, S.-I., 2016. Seismological detection of low velocity anomalies surrounding the mantle transition zone in Japan subduction zone. Geophys. Res. Lett. 43, 2480–2487.

Makhluf, A.R., Newton, R.C., Manning, C.E., 2016. Hydrous albite magmas at lower crustal pressure: new results on liquidus H_2O content, solubility, and H_2O activity in the system $NaAlSi_3O_8$-H_2O-NaCl at 1.0 GPa. Contrib. Mineral. Petrol. 171, 75.

Malavergne, V., Bureau, H., Raepsaet, C., Gaillard, F., Poncet, M., Surble, S., Sifr, D., Shcheka, S., Fourdrin, C., Deldicque, D., 2019. Experimental constraints on the fate of H and C during planetary core-mantle differentiation. Implications for the Earth. Icarus 321, 473–485.

Manning, C.E., 2018. The influence of pressure on the properties and origins of hydrous silicate liquids in Earth's interior. In: Kono, Y., Sanloup, C. (Eds.), Magmas Under Pressure: Advances in High-Pressure Experiments on Structure and Properties of Melts. Cambridge, pp. 83–114.

Monteux, J., Andrault, D., Samuel, H., 2016. On the cooling of a deep terrestrial magma ocean. Earth Planet. Sci. Lett. 448, 140–149.

Mookherjee, M., Stixrude, L., Karki, B.B., 2008. Hydrous silicate melt at high pressure. Nature 452, 983–986.

Mysen, B.O., Eggler, D.H., Seitz, M.G., Holloway, J.R., 1976. Carbon dioxide in silicate melts and crystals. Part I: solubility measurements. Am. J. Sci. 276, 455–479.

Mysen, B.O., Kumamoto, K., Cody, G.D., Fogel, M.L., 2011. Solubility and solution mechanisms of C-O-H volatiles in silicate melt with variable redox conditions and melt composition at upper mantle temperatures and pressures. Geochim. Cosmochim. Acta 75, 6183–6199.

Nowak, M., Porbatzki, D., Spickenbom, K., Diedrich, O., 2003. Carbon dioxide speciation in silicate melts: a restart. Earth Planet. Sci. Lett. 207, 131–139.

O'Neill, H.St.C., 1991. The origin of the Moon and the early history of the Earth – a chemical model. Part 2: The Earth. Geochim. Cosmochim. Acta 55, 1159–1172.

Papale, P., Moretti, R., Barbato, D., 2006. The compositional dependence of the saturation surface of H_2O + CO_2 fluids in silicate melts. Chem. Geol. 229, 78–95.

Revenaugh, J., Sipkin, S.A., 1994. Seismic evidence for silicate melt atop the 410-km mantle discontinuity. Nature 369, 474–476.

Righter, K., Drake, M.J., 1999. Effect of water on metal-silicate partitioning of siderophile elements: a high pressure and temperature terrestrial magma ocean and core formation. Earth Planet. Sci. Lett. 171, 383–399.

Rohrbach, A., Schmidt, M.W., 2011. Redox freezing and melting in the Earth's deep mantle resulting from carbon–iron redox coupling. Nature 472, 209–212.

Rubie, D.C., Melosh, H., Reid, J., Liebske, C., Righter, K., 2003. Mechanisms of metal–silicate equilibration in the terrestrial magma ocean. Earth Planet. Sci. Lett. 205, 239–255.

Rüpke, L., Morgan, J.P., Hort, M., Connolly, J.A.D., 2004. Serpentine and the subduction zone water cycle. Earth Planet. Sci. Lett. 223, 17–34.

Sakamaki, T., Ohtani, E., Urakawa, S., Terasaki, H., Katayama, Y., 2011. Density of carbonated peridotite magma at high pressure using an X-ray absorption method. Am. Mineral. 96, 553–557.

Sakamaki, T., 2017. Density of hydrous magma. Chem. Geol. 475, 135–139.

Schmandt, B., Jacobsen, S.D., Becker, T.W., Liu, Z., Dueker, K.G., 2014. Dehydration melting at the top of the lower mantle. Science 344, 1265–1268.

Solomatova, N.V., Caracas, R., Manning, C.E., 2019. Carbon sequestration during core formation implied by complex carbon polymerization. Nat. Commun. 10, 789.

Stagno, V., Ojwang, D.C., McCammon, C.A., Frost, D.J., 2013. The oxidation state of the mantle and the extraction of carbon from Earth's interior. Nature 493, 84–88.

Stixrude, L., De Koker, N., Sun, N., Mookherjee, M., Karki, B.B., 2009. Thermodynamics of silicate liquids in the deep Earth. Earth Planet. Sci. Lett. 278, 226–232.

Stolper, E., 1982. The speciation of water in silicate melts. Geochim. Cosmochim. Acta 46, 2609–2620.

Tateno, S., Hirose, K., Ohishi, Y., 2014. Melting experiments on peridotite to lowermost mantle conditions. J. Geophys. Res., Solid Earth 119, 4684–4694.

Toffelmier, D.A., Tyburczy, J.A., 2007. Electromagnetic detection of a 410-km-deep melt layer in the southwestern United States. Nature 447, 991–994.

Tonks, W.B., Melosh, H.J., 1993. Magma ocean formation due to giant impacts. J. Geophys. Res., Planets 98, 5319–5333.

Vuilleumier, R., Seitsonen, A.P., Sator, N., Guillot, B., 2015. Carbon dioxide in silicate melts at upper mantle conditions: insights from atomistic simulations. Chem. Geol. 418, 77–88.

Williams, Q., Garnero, E.J., 1996. Seismic evidence for partial melt at the base of Earth's mantle. Science 273, 1528–1530.